

Enhanced Regional Ocean Ensemble Data Assimilation Through Atmospheric Coupling in the SKRIPS Model

Rui Sun¹, Sivareddy Sanikommu², Aneesh C. Subramanian³, Matthew R. Mazloff¹, Bruce D. Cornuelle¹, Ganesh Gopalakrishnan¹, Arthur J. Miller¹, Ibrahim Hoteit³

¹Scripps Institution of Oceanography, California, USA

²Physical Sciences and Engineering Division, King Abdullah University of Science and Technology (KAUST), Thuwal, Saudi Arabia

³Department of Atmospheric and Oceanic Sciences, University of Colorado Boulder, Colorado, USA

Key Points:

- We implement an ocean ensemble data assimilation system using the SKRIPS ocean-atmosphere coupled model for the Red Sea region.
- The diversity of the atmospheric forcing is an important part of ensemble spread in the ocean model.
- A downscaled ensemble generated by the coupled model performs as well or better than an ocean model ensemble generated with ECMWF ensemble forcing.

Corresponding author: Rui Sun, rus043@ucsd.edu

Abstract

We investigate the impact of ocean data assimilation using the Ensemble Adjustment Kalman Filter (EAKF) from the Data Assimilation Research Testbed (DART) on the oceanic and atmospheric states of the Red Sea. Our study extends the ocean data assimilation experiment performed by Sanikommu et al. (2020) by utilizing the SKRIPS model coupling the MITgcm ocean model and the Weather Research and Forecasting (WRF) atmosphere model. Using a 50-member ensemble, we assimilate satellite-derived sea surface temperature and height and in-situ temperature and salinity profiles every three days for one year, starting January 01 2011. Atmospheric data are not assimilated in the experiments. To improve the ensemble realism, perturbations are added to the WRF model using several physics options and the stochastic kinetic energy backscatter (SKEB) scheme. Compared with the control experiments using uncoupled MITgcm with ECMWF ensemble forcing, the EAKF ensemble mean oceanic states from the coupled model are better or insignificantly worse (root-mean-square errors are 30% to -2% smaller), especially when the atmospheric model uncertainties are accounted for with stochastic perturbations. We hypothesize that the ensemble spreads of the air-sea fluxes are better represented in the downscaled WRF ensembles when uncertainties are well accounted for, leading to improved representation of the ensemble oceanic states in EAKF. Although the feedback from ocean to atmosphere is included in this two-way regional coupled configuration, we find no significant effect of ocean data assimilation on the ensemble mean latent heat flux and 10-m wind speed over the Red Sea. This suggests that the improved skill using the coupled model is not from the two-way coupling, but from downscaling the ensemble atmospheric forcings (one-way coupled) to drive the ocean model.

Plain Language Summary

We investigate how combining ocean information accounting for weather processes can help us better understand and predict the ocean-atmospheric state of the Red Sea. We use a coupled ocean and atmosphere model to assimilate satellite and ship-based ocean observations. We assess the performance of the assimilation system using fifty different realizations of the atmospheric state and found that it improves the prediction of oceanic state compared to using the ocean model alone for assimilation and prediction. This success is because the combined ocean-atmosphere model provides a broader range of possible ocean conditions. We also look at how incorporating ocean observation information may potentially impact weather forecasts in the coupled model.

1 Introduction

Numerical models have been used to analyze and predict ocean states for decades. Realistically configured numerical models can simulate oceanic conditions that are generally consistent with observations, but there can be substantial differences when comparing with observations at specific times and locations (Edwards et al., 2015). Even with a perfect model, the differences can result from uncertainties of initial conditions, perturbations, parameterizations, and forcings. Because of this, data assimilation (DA) is used to constrain the model solutions using observational data, including observation uncertainty and model representational error (Edwards et al., 2015).

The Ensemble Kalman Filter (hereafter EnKF) provides an efficient framework for ocean data assimilation (Evensen, 1994). It has gained popularity because of its simple conceptual formulation and relative ease of implementation, requiring no derivation of tangent linear or adjoint models, with only forward model integration in time (Evensen, 2003). Furthermore, its computational requirements scale with ensemble size, and so can be affordable and comparable with other popular sophisticated assimilation methods (Evensen, 2003). EnKF based data assimilation systems have been developed for many applications. For example, Evensen and Van Leeuwen (1996) assimilated altimeter data in the

67 Agulhas region using a quasi-geostrophic model; Sakov et al. (2012) and Hoteit et al. (2013)
68 respectively produced realistic estimates of the ocean circulation in the North Atlantic
69 and the Gulf of Mexico; Sanikommu et al. (2020) investigated the impact of atmospheric
70 forcing and model physics perturbations using an Ensemble Adjustment Kalman Filter (EAKF).
71 In addition to ocean data assimilation, EnKF is used for operational atmospheric assim-
72 ilation at the Canadian Meteorological Centre (Houtekamer et al., 2005) among many
73 other applications (e.g., Lawson & Hansen, 2004; Leeuwenburgh et al., 2005; Bannister,
74 2017).

75 A major component of EnKF data assimilation systems is the background error
76 covariance estimated from the ensembles (Bannister, 2008a, 2008b; Song et al., 2010).
77 EnKFs can suffer from the collapse of the ensemble spread, which unrealistically reduces
78 the background error covariance in the data assimilation system (e.g., J. Anderson & An-
79 derson, 1999; Hoteit et al., 2002). This is often mitigated using covariance inflation tech-
80 niques to increase the ensemble spread to better describe the background covariance (J. An-
81 derson & Anderson, 1999; Hoteit et al., 2002; F. Zhang et al., 2004; Whitaker & Hamill,
82 2012; Luo & Hoteit, 2012). A more representative approach is to account directly for un-
83 certainties in the model, such as the forcing and boundary conditions. Diverse high-resolution
84 forcings that represent the uncertainty of the atmosphere are indeed desirable for ocean
85 ensemble data assimilation system. Many studies have demonstrated improved forecasts
86 and analyses when driving ensemble ocean data assimilation systems with perturbed at-
87 mospheric forcing (Lisæter et al., 2003; Evensen, 2004; Wan et al., 2008; Shu et al., 2011;
88 Sakov et al., 2012; Karspeck et al., 2013; Penny et al., 2015; Sanikommu et al., 2017, 2019).
89 Others investigated the perturbed model physics (Sandery et al., 2014; Brankart et al.,
90 2015; Lima et al., 2019), or combined the perturbations of atmospheric forcing and model
91 physics (Vandenbulcke & Barth, 2015; K. M. Kwon et al., 2016; Sanikommu et al., 2020).
92 A recent study by Sanikommu et al. (2020) performed a detailed analysis of the impacts
93 of model physics perturbations and atmospheric forcing on a high-resolution regional ocean
94 DA system. The DA experiments improved the forecasts of oceanic states by using mul-
95 tiple oceanic model physics and ensemble atmospheric forcing now available from oper-
96 ational weather systems.

97 Our study takes a step forward toward a fully coupled ocean–atmospheric data as-
98 similation system, with application to the Red Sea region. A regional assimilation sys-
99 tem is crucial for improving forecasts in the Red Sea due to its unique characteristics in
100 terms of both oceanic and atmospheric conditions (Hoteit et al., 2021). The region is prone
101 to dust and sandstorms, particularly during the transitional seasons of spring and au-
102 tumn, originating from nearby deserts like the Sahara. These storms significantly reduce
103 visibility and impact air quality (Prakash et al., 2014). The Red Sea also experiences fre-
104 quent temperature inversions, especially in winter, which affect temperature profiles, pol-
105 lutant dispersal, and vertical mixing of air masses. The region is influenced by two pri-
106 mary wind patterns: the Southwest Monsoon, bringing humid air and thunderstorms,
107 and the Northwest Monsoon, bringing drier air (Langodan et al., 2017). A sea breeze
108 often develops during the day, cooling coastal areas (Davis et al., 2019). The Red Sea
109 warm surface waters contribute to high levels of water vapor, impacting local weather
110 conditions and precipitation. The local atmospheric features vary significantly with sea-
111 sons, weather patterns, and local geography (Dasari et al., n.d.). The Red Sea holds eco-
112 nomic importance and plays a vital role in international trade. Further, the Red Sea cir-
113 culation plays a dominant role in modifying the salinity budgets of the western Indian
114 Ocean. Global reanalysis often fails to capture the Red Sea circulation features accurately
115 due to coarse resolutions and limited observations (Sanikommu et al., 2023a). Develop-
116 ing a high-resolution regional reanalysis using local observations and coupled ocean–atmospheric
117 data assimilation system would greatly enhance the forecasts in the Red Sea, and this
118 is important for many applications in this unique region.

119 In this context, we implement a new ensemble DA system for the Red Sea using
 120 the Scripps–KAUST Regional Integrated Prediction System (SKRIPS, Sun et al., 2019,
 121 2023) and the Data Assimilation Research Testbed (DART, J. Anderson et al., 2009).
 122 This work is an extension of previous DA efforts for the Red Sea (Toye et al., 2017; Sanikommu
 123 et al., 2020, 2023b), replacing the uncoupled ocean model with the SKRIPS coupled model (Sun
 124 et al., 2019, 2023). Here we assimilate only oceanic observations using the DART–EAKF
 125 system and investigate the estimated oceanic and atmospheric states of the Red Sea re-
 126 gional coupled model, using different options to perturb the physics of the atmosphere
 127 model. We evaluate the performance of the coupled model in forecasting the oceanic states,
 128 the impact of atmospheric model physics options on the coupled model, and the feed-
 129 back of the ocean data assimilation to the atmospheric model. Although we only assim-
 130 ilate ocean observations in this work, the present study is a step toward developing a weakly
 131 coupled DA system and operational analysis and forecasting system for the Red Sea. Be-
 132 cause the random atmospheric states are generated by perturbing the model physics when
 133 using a coupled model, there is less need to generate large ensembles of atmospheric forc-
 134 ings (Sanikommu et al., 2023a), enhancing the robustness of the DA system.

135 The rest of the manuscript is organized as follows. We first introduce the ensem-
 136 ble DA system and its implementation in Section 2. The results of the DA experiments
 137 are presented and discussed in Section 3. The final section outlines the main findings and
 138 concludes this work.

139 2 Implementations and Experimental Design

140 2.1 The Data Assimilation Framework

141 We use the SKRIPS model (Sun et al., 2019) for the coupled simulation: the oceanic
 142 model component is the MIT general circulation model (MITgcm, Marshall et al., 1997;
 143 Campin et al., 2019) and the atmospheric model component is the Weather Research and
 144 Forecasting (WRF) model (Skamarock et al., 2019). The Earth System Modeling Frame-
 145 work (ESMF, Hill et al., 2004) and the National United Operational Prediction Capa-
 146 bility (NUOPC) layer are used to handle the coupling between MITgcm and WRF. The
 147 schematic diagram of the DART–SKRIPS framework and the domain used in the exper-
 148 iment are shown in Fig. 1. The ocean data are assimilated using EAKF available from
 149 the DART–MITgcm package (Hoteit et al., 2013, 2015), aiming to evaluate their impact
 150 on the ocean and atmosphere states in the coupled system. The ROCOTO workflow (Harrop
 151 et al., 2017) is used for the management of the pre- and post-processing scripts in the
 152 developed DART–SKRIPS framework.

153 The coupled model is also described in the diagram shown in Fig. 1. In the cou-
 154 pling process, MITgcm sends sea surface temperature (SST) and ocean surface veloc-
 155 ity to WRF; WRF sends air-sea flux and surface atmospheric fields to MITgcm, includ-
 156 ing (1) net surface longwave and shortwave radiative fluxes, (2) surface latent and sen-
 157 sible heat fluxes, (3) 10-m wind speed, (4) precipitation, and (5) evaporation. The MIT-
 158 gcm model uses the surface atmospheric variables to prescribe surface forcing, includ-
 159 ing (1) total net surface heat flux, (2) surface wind stress, and (3) freshwater flux. The
 160 total net surface heat flux is computed by adding surface latent heat flux, sensible heat
 161 flux, net shortwave radiation flux, and net longwave radiation flux. The surface latent
 162 and sensible heat fluxes are computed using the COARE 3.0 bulk algorithm in WRF (Fairall
 163 et al., 2003).

164 2.2 Experimental Design

165 To study the impact of ocean data assimilation on the oceanic and atmospheric states,
 166 we perform a series of 50-member ensemble DA experiments using coupled and uncou-
 167 pled models starting from January 01 2011, assimilating the observational data every 3

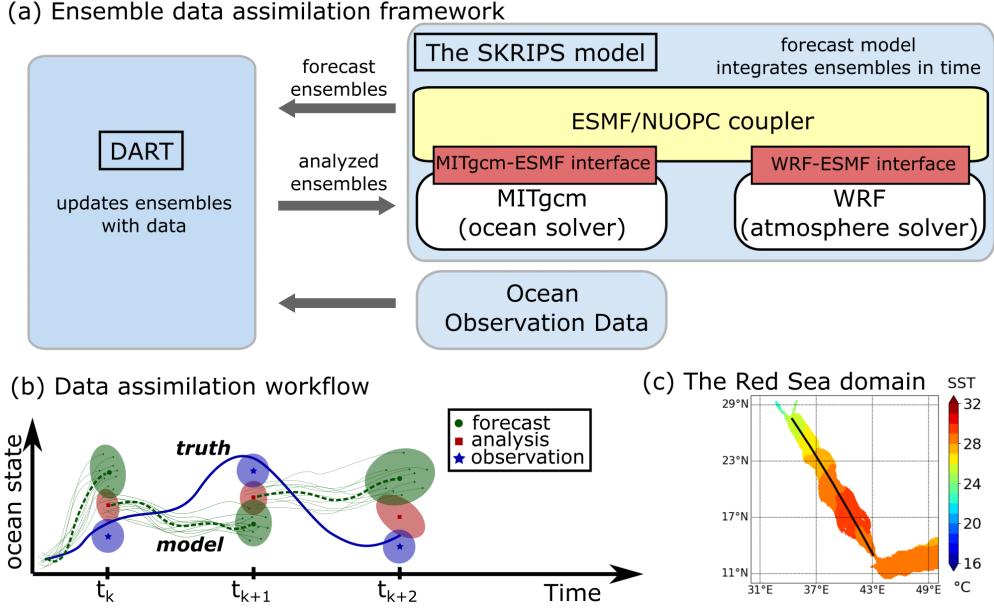


Figure 1. The schematic description of the DART-SKRIPS data assimilation system. Panel (a) indicates the DART-SKRIPS framework: the blue blocks denote the SKRIPS model, DART, and ocean observations; the yellow block is the ESMF/NUOPC coupler; the white blocks are the ocean and atmosphere components; the red blocks are the implemented MITgcm-ESMF and WRF-ESMF interfaces. The arrows indicate the information exchange between DART and SKRIPS. Panel (b) shows the workflow at three time steps: the thick solid line indicates the evolution of the “truth”; the dashed line indicates the ensemble averaged forecast; the thin solid lines indicate the evolution of the ensemble members; the red dots indicate the analysis; the shaded areas indicate the error covariance; t_k , t_{k+1} , and t_{k+2} indicate three steps when observational data are assimilated. Panel (c) shows the domain of the coupled model, with the black line indicating the centerline of the Red Sea.

168 days. For the coupled model experiments, the ocean and atmosphere models are nested
 169 in GLORYS and ERA5 reanalyses, respectively. For the uncoupled model experiments,
 170 the ocean model is also nested in GLORYS, but driven by ECMWF derived atmospheric
 171 forcing. Further details on the initial and boundary conditions will be discussed in the
 172 latter sections. The same setup is used for the ocean model, but different options are used
 173 for the atmosphere in the 50-member ensemble DA experiments:

- 174 1. OCN.daO uses only the ocean model forced by the ECMWF ensemble mean.
- 175 2. OCN.daF uses only the ocean model forced by the 50-member ECMWF ensem-
 176 bles.
- 177 3. CPL.daO uses the coupled model with no perturbations to the atmosphere.
- 178 4. CPL.daS uses the coupled model with stochastic forcings in the atmospheric model.
- 179 5. CPL.daP uses the coupled model with perturbed physics options in the atmospheric
 180 model (e.g., microphysics, convection, and planetary boundary layer).
- 181 6. CPL.daSP uses the coupled model with stochastic forcings and perturbed atmo-
 182 sphere physics options.

183 OCN.daO and OCN.daF follow the experiments using the ocean-only models in Sanikommu
 184 et al. (2020), but without inflation to investigate the changes using the coupled model.
 185 They also serve as benchmarks to evaluate the performance of the coupled experiments.
 186 In the coupled DA experiment CPL.daO, although we did not perturb the atmospheric

187 model physics, the randomness of the atmospheric forcing is from the feedback of dif-
 188 ferent ocean states. Different random seeds are used for the stochastic model in CPL.daS
 189 and CPL.daSP from 1 to 50. The coupled DA experiments OCN.daS, OCN.daP, and OCN.daSP
 190 are conducted to assess the effect of different strategies of the atmospheric forcings, and
 191 thus we did not assimilate the atmospheric observational data in our experiments. Al-
 192 though the ocean feedback is important in the coupled model, we did not perform DA
 193 experiments driven by the atmospheric forcings from stand-alone WRF models because
 194 it is out of the scope of our work.

195 **2.3 The Forward Models**

196 The initial conditions, boundary conditions, and forcings are outlined in Table 1.
 197 The MITgcm initial conditions are obtained from a spin-up run as described in Sanikommu
 198 et al. (2020), with randomly selecting 50 ocean states corresponding to ± 15 days from
 199 the initial time. The boundary conditions for the ocean are updated by linearly inter-
 200 polating between the daily data from Global Ocean Reanalysis and Simulation (GLORYS,
 201 Jean-Michel et al., 2021). For the uncoupled experiments, the atmospheric forcings are
 202 from the ECMWF atmospheric ensemble from The Observing System Research and Pre-
 203 dictability Experiment Interactive Grand Global Ensemble project (TIGGE, Bougeault
 204 et al., 2010), with full details available in Buizza (2014). We combined the fields of the
 205 00 and 12 UTC TIGGE initial conditions and 06 and 18 UTC forecasts as 6-hourly forc-
 206 ing for our ocean ensemble assimilation runs. For OCN.daO, we forced the model with
 207 the ensemble mean of the atmospheric forcings; for OCN.daF, we forced the model with
 208 the ECMWF 50-member ensembles. In the coupled experiments, ERA5 provides the ini-
 209 tial and boundary conditions for the atmosphere model, with the atmospheric bound-
 210 ary conditions updated by linearly interpolating between the 6-hourly fields. Spectral
 211 nudging is not used in the DA experiments because (1) nudging may constrain the high
 212 frequency internal variability of the atmosphere model and (2) the domain size is com-
 213 parable with wavelengths typically used in the spectral nudging simulations (Liu et al.,
 214 2012).

215 We choose the latitude–longitude (cylindrical equidistant) map projection to gener-
 216 ate the grids for MITgcm and WRF. The domains for both models extend from 10°N
 217 to 30°N and from 30°E to 50°E . In the ocean model, the horizontal grid has 500×500
 218 (lat \times long) cells and the spacing is about 4 km; in the atmospheric model, the horizon-
 219 tal grid has 125×125 (lat \times long) cells and the spacing is about 16 km. There are 40 sigma
 220 layers in the atmospheric model (top pressure is 50 hPa) and 50 z-layers in the ocean
 221 model ($dz = 4$ m at the top). The time step of the oceanic model is 200 seconds; the
 222 time step of the atmospheric model is 25 seconds; the coupling interval is 200 seconds.

223 **2.4 Model Perturbations**

224 For the oceanic simulations in all DA experiments, we use various physical param-
 225 eterization schemes to account for the effects of unresolved scales of motion as proposed
 226 by Sanikommu et al. (2020), summarized in Table 2. Three different categories of model
 227 physics are selected: horizontal viscosity, vertical mixing, and horizontal diffusion. We
 228 include three different horizontal viscosity schemes: the simple harmonic scheme, the sim-
 229 ple biharmonic of Holland (1978), and the Smagorinsky/Leith scheme (Smagorinsky et
 230 al., 1993; Griffies & Hallberg, 2000) with the coefficients suggested in the literature (Leith,
 231 1996; Griffies & Hallberg, 2000). For vertical mixing, four different schemes are included:
 232 the nonlocal K-Profile Parameterization (KPP) scheme (W. G. Large et al., 1994), the
 233 PP81 scheme (Pacanowski & Philander, 1981), the MY82 scheme (Mellor & Yamada,
 234 1982), and the GGL90 scheme (Gaspar et al., 1990). For the horizontal diffusion, we use
 235 implicit diffusion, simple-explicit harmonic diffusion, and three different flavors of Gent-
 236 McWilliams/Redi subgrid-scale eddy parameterization schemes (hereafter GMREDI, Gent
 237 & McWilliams, 1990; Gent et al., 1995; Redi, 1982): the GMREDI clipping scheme of Cox

238 (1987), the GMREDI-dm95 tapering scheme of Danabasoglu and McWilliams (1995),
 239 and the GMREDI-dd92 tapering scheme of W. Large et al. (1997). Table 2 lists the co-
 240 efficients used in these schemes.

241 We also perturb the physics options in WRF to parameterize microphysics, con-
 242 vection, and planetary boundary layer (PBL), summarized in Table 3. For the micro-
 243 physics we use the Morrison 2-moment scheme (Morrison et al., 2009), the Purdue-Lin
 244 scheme (Chen & Sun, 2002), the Thompson scheme (Thompson et al., 2008), the WRF
 245 single moment 6-class scheme (Hong & Lim, 2006), and the WRF double moment 6-class
 246 scheme (Lim & Hong, 2010). For the cumulus convection, we use the Kain-Fritsch scheme (Kain,
 247 2004), the Betts-Miller-Janjic scheme (Janjić, 1994), the Grell-Freitas Ensemble scheme (Grell
 248 & Freitas, 2014), the new Tiedtke scheme (C. Zhang & Wang, 2017), and the simplified
 249 Arakawa-Schubert scheme (Y. C. Kwon & Hong, 2017). For the planetary boundary layer,
 250 we use the Mellor-Yamada Nakanishi Niino scheme (MYNN, Nakanishi & Niino, 2004,
 251 2009), the Yonsei University scheme (Hong et al., 2006), and the Mellor-Yamada-Janjic
 252 scheme (Janjić, 1994). The radiation and land surface schemes are not perturbed: the
 253 Rapid Radiation Transfer Model for GCMs (RRTMG, Iacono et al., 2008) is used for long-
 254 wave and shortwave radiation transfer through the atmosphere; the Noah land surface
 255 model is used for the land surface processes (Tewari et al., 2004). The physics scheme
 256 perturbation is based on the ensemble forecast system of the Center For Western Weather
 257 and Water Extremes (CW3E, Oakley et al., 2023). For the experiments without perturb-
 258 ing the atmospheric model (i.e., CPL.daO and CPL.daS), we use Morrison 2-moment
 259 scheme, Kain-Fritsch scheme, and MYNN scheme for microphysics, convection, and PBL,
 260 respectively.

261 In addition to perturbing the atmospheric model physics, we used the SKEB scheme (Shutts,
 262 2005; Berner et al., 2009) to account for the unrepresented uncertainties in the model.
 263 This scheme adds stochastic, small-amplitude perturbations to the horizontal wind and
 264 potential temperature. The default amplitudes of the stochastic perturbations in WRF
 265 were used in CPL.daS and CPL.daSP, which were able to provide more reliable ensem-
 266 ble spreads (Berner et al., 2011, 2015).

267 2.5 Data Used in Assimilation and Validation

268 We assimilate data from level-4 SST blended daily product available on a $0.25^\circ \times$
 269 0.25° grid (Reynolds et al., 2007; Banzon et al., 2016), along-track satellite altimeter level-
 270 3 sea level anomalies (SLAs; corrected for dynamic atmospheric loading, ocean tide, and
 271 long wavelength errors) available from Copernicus Marine Environment Monitoring Ser-
 272 vice (here after CMEMS-L3, Mertz et al., 2017), and quality controlled in situ glider tem-
 273 perature and salinity profiles from EN4 data (Ingleby & Huddleston, 2007; Good et al.,
 274 2013). The in situ temperature and salinity profiles are sparse, and there are only 244
 275 temperature and 110 salinity profiles in the entire year 2011 from the glider in the Red
 276 Sea. Errors associated with these observations are assumed uncorrelated, so the obser-
 277 vational error covariance matrix is diagonal. The combined observation and represen-
 278 tation error variance is determined based on previous DA experiments (Toye et al., 2017;
 279 Sanikommu et al., 2020) and accounts for errors due to: measurement devices, omitted
 280 processes, unresolved subgrid scale dynamics, and numerical errors in interpolation. Tem-
 281 porally static, partially homogeneous, and depth independent observational error vari-
 282 ance values of $(0.5^\circ\text{C})^2$, $(0.04\text{ m})^2$, $(0.5^\circ\text{C})^2$, and $(0.3\text{ psu})^2$ are then used for satellite
 283 SST, satellite along-track SLA, in situ temperature and salinity, respectively. A cutoff
 284 radius of about 300 km was imposed to localize the impact the observations in the hor-
 285 izontal directly (not in the vertical) as a way to mitigate spurious correlations.

286 For validation, we evaluate the daily averaged ocean forecasts and analyses as re-
 287 sulting from the DA experiments. We first use the assimilated data to examine the time
 288 series of innovations and residuals. In addition to the assimilated data, independent ob-

Table 1. The computational domain, WRF physics schemes, initial condition, boundary condition, and forcing terms used in the present simulations.

	OCN Experiments	CPL Experiments
Model region	10°N to 30°N; 30°E to 50°E	
Grid size	500×500	500×500 for ocean 125×125 for atmosphere
Grid spacing	0.04° × 0.04°	0.04° × 0.04° for ocean 0.16° × 0.16° for atmosphere
Microphysics scheme		Various (see Table 3)
Convection scheme		Various (see Table 3)
PBL scheme	Not necessary	Various (see Table 3)
Longwave radiation scheme		RRTMG
Shortwave radiation scheme		RRTMG
Land surface scheme		Noah land surface model
Vertical levels	50 (ocean only)	40 (atmosphere) 50 (ocean)
Initial and boundary conditions	GLORYS (ocean only)	ERA5 (atmosphere) GLORYS (ocean)
Atmospheric forcings for oceanic model	From ECMWF TIGGE product	From WRF

Table 2. MITgcm model physics parameterizations in the present study.

Horizontal Viscosity	Vertical Mixing	Horizontal Diffusion
Simple Harmonic (30 m ² /s)	K-Profile Parameterization	Implicit Diffusion
Simple Biharmonic (10 ⁷ m ⁴ /s)	PP81	Explicit Diffusion (100 m ² /s)
SMAGLEITH-Harmonic (30 m ² /s), Smag Coeff 2.5, and Leith Coeff 1.85	MY82	GMREDI-clipping (100 m ² /s)
	GGL90	GMREDI-dm95 (100 m ² /s) GMREDI-dd92 (100 m ² /s)

Table 3. WRF model physics parameterizations in the present study. The physics options used in the experiments without perturbing the model physics (i.e., CPL.daO and CPL.daS) are highlighted using bold red color.

Microphysics	Convection	Planetary Boundary Layer
Morrison 2-moment	Kain–Fritsch	Mellor–Yamada Nakanishi Niino
Purdue-Lin	Betts–Miller–Janjic	Yonsei University
Thompson	Grell–Freitas Ensemble	Mellor–Yamada–Janjic
WRF single moment 6-class	New Tiedtke	
WRF double moment 6-class	Simplified Arakawa–Schubert	

289 observations are used. To analyze the subsurface features, we use 206 profiles of temper-
 290 ature and salinity collected between September 15 to October 08 2011 by a joint Woods
 291 Hole Oceanography Institute (WHOI) and King Abdullah University of Science and Tech-
 292 nology (KAUST) cruise along the eastern part of the Red Sea, collected with a horizon-
 293 tal spacing of 10 km (Zhai et al., 2015). We also use other satellite products to evalu-
 294 ate the DA results. For SST we select the high-resolution daily averaged level 4 SST prod-
 295 uct from the Operational Sea Surface Temperature and Sea Ice Analysis (OSTIA, Stark
 296 et al., 2007; Donlon et al., 2012) because it is mapped differently with higher resolution.
 297 For sea surface height (SSH) we use multimission altimeter merged satellite level 4 grid-
 298 ded absolute dynamic topography (ADT) provided by CMEMS (hereafter CMEMS-L4,
 299 Mertz et al., 2017). Compared with the assimilated CMEMS-L3 data, the CMEMS-L4
 300 data is gridded on a 0.25° grid and thus can be used to estimate the errors across the
 301 entire Red Sea region. The SSH anomaly from the DA experiments is the instantaneous
 302 SSH obtained in the simulations minus the time-averaged SSH from the 15-year MIT-
 303 gcm model in Sanikommu et al. (2020). The SSH anomalies in CMEMS-L3 and CMEMS-
 304 L4 are the sea level height above the mean surface based on the long-term averaged ob-
 305 servations between 1993 to 2012. Because of the lack of in situ observational data of the
 306 atmosphere, we use ERA5 to validate the latent heat fluxes and wind speed simulated
 307 by the coupled experiments.

308 **3 Results**

309 The results obtained from the DA experiments are presented in this section. First,
 310 we analyze the ensemble spread of the atmospheric forcings and sea surface temperature.
 311 Then we examine the ocean states (e.g., SST, SSH, and vertical profiles) to assess the
 312 impact of atmospheric forcings in the uncoupled and coupled systems using the valida-
 313 tion data. In addition to the ocean states, the air-sea exchanges (e.g., latent heat flux)
 314 and surface atmospheric states (e.g., wind speed) are also analyzed to illustrate the feed-
 315 back from the ocean to the atmosphere due to assimilation. Finally, we discuss the changes
 316 in the ocean dynamics from assimilating the observation data.

317 **3.1 Ensemble Spread Analysis**

318 Similarly to the DA experiments in Sanikommu et al. (2020), we hypothesize that
 319 the estimated ocean states are improved when uncertainties in various sources are well
 320 accounted for. Incorporating uncertainties in the system improves ensemble spreads in
 321 the ocean systematically. For instance, Figs. 2 and 3 display the temporal evolution of
 322 atmospheric forcing root-mean-square (RMS) spread in the DA experiments, except for
 323 OCN.daO which is forced by the ECMWF ensemble mean. The spread in OCN.daF is
 324 from the ECMWF ensemble atmospheric forcing; others are from the coupled model out-
 325 puts. In comparison with OCN.daF, the spread in CPL.daO is smaller by about one or-
 326 der of magnitude because the atmospheric models are not perturbed and the spread of
 327 atmosphere is from the ocean perturbations. When the SKEB scheme is applied in CPL.daS
 328 and CPL.daSP, the spread of the atmospheric forcing is larger than that in OCN.daF,
 329 which in turn increases the SST spread, shown in Fig. 4. The impact of the atmospheric
 330 forcings on the ocean states will be detailed in the latter sections.

331 **3.2 Sea Surface Temperature**

332 We analyze the SST obtained in our DA experiments to assess its sensitivity to the
 333 atmospheric perturbations. The root-mean-square-errors (RMSEs) between the SST anal-
 334 yses and observations in all DA experiments are shown in Fig. 5 and summarized in Ta-
 335 ble 4. The best SST forecast and analysis are both from experiment CPL.daSP, when
 336 the SKEB scheme is turned on and the WRF physics options are perturbed. The SSTs
 337 obtained in the coupled experiments (CPL.daS, CPL.daP, and CPL.daSP; except for the

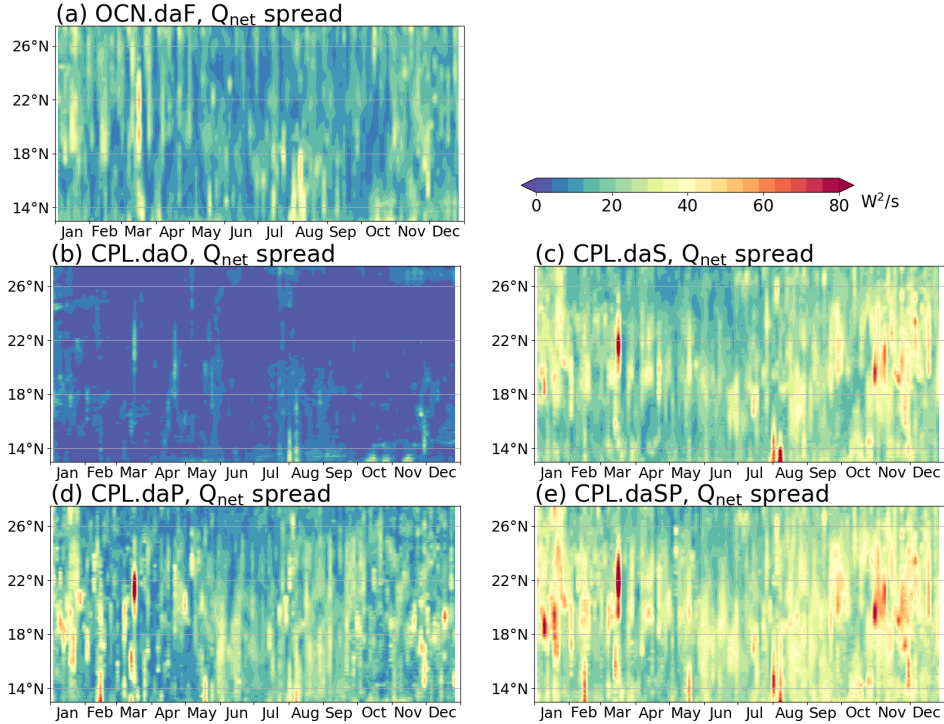


Figure 2. The spatial and temporal evolution of the RMS spread of net surface heat flux Q_{net} along the center line of the Red Sea shown in Fig. 1(c). The Q_{net} is calculated by summing up the latent heat flux, sensible heat flux, net surface shortwave fluxes, and net surface longwave fluxes. Panel (a) shows the spread in the ocean-only experiment driven by ECMWF derived forcing; Panel (b-e) show the spread in the coupled experiments with no perturbations, only SKEB, only perturbed model physics, and SKEB + perturbed model physics, respectively.

338 benchmark case CPL.daO) are better than that of the uncoupled experiment OCN.daF,
 339 with improvements more than twice larger than standard error of the mean SST from
 340 CPL.daSP (about 0.015°C , the standard deviation of SST divided by the square-root
 341 of the number of ensemble members). Better improvements are obtained when using only
 342 the stochastic forcings (CPL.daS) compared with only perturbing the WRF physics (CPL.daP),
 343 but this difference is less significant (smaller than 0.015°C). Although the perturbations
 344 in the atmospheric forcing are small in CPL.daO (shown in Figs. 2 and 3), the RMSE
 345 errors of SST forecasts and analyses are improved compared to the benchmark exper-
 346 iment OCN.daO by 0.156°C and 0.101°C , respectively. This indicates that small per-
 347 turbations of the atmospheric forcing can improve SST in the DA experiments.

348 Figure 5 shows that the RMSEs of SST forecasts and analyses increase in summer
 349 for the benchmark runs (i.e., OCN.daO and CPL.daO), but RMSEs get smaller when
 350 using the coupled model (i.e., CPL.daS, CPLdaP, and CPL.daSP). In this season, the
 351 SST has a larger spread in all the experiments, similar to the results shown in Sanikommu
 352 et al. (2020), likely because the ocean is more sensitive to heat fluxes when the mixed
 353 layer depth is shallower.

354 In addition to the assimilated data, we validated the SSTs using the OSTIA SST.
 355 The RMSEs and correlations are shown in Fig. 6 and summarized in Table. 4. We present
 356 the SST correlations to evaluate the forecast of the SST evolution during the year. It
 357 can be seen that the SST obtained in CPL.daSP has larger correlations and smaller RM-
 358 SEs in the north Red Sea, center Red Sea, and Gulf of Aden regions. Compared with
 359 the uncoupled experiment OCN.daF, the coupled experiment CPL.daSP has a smaller
 360 RMSE by 0.035°C (6.5%, more than twice the standard error). On the other hand, the

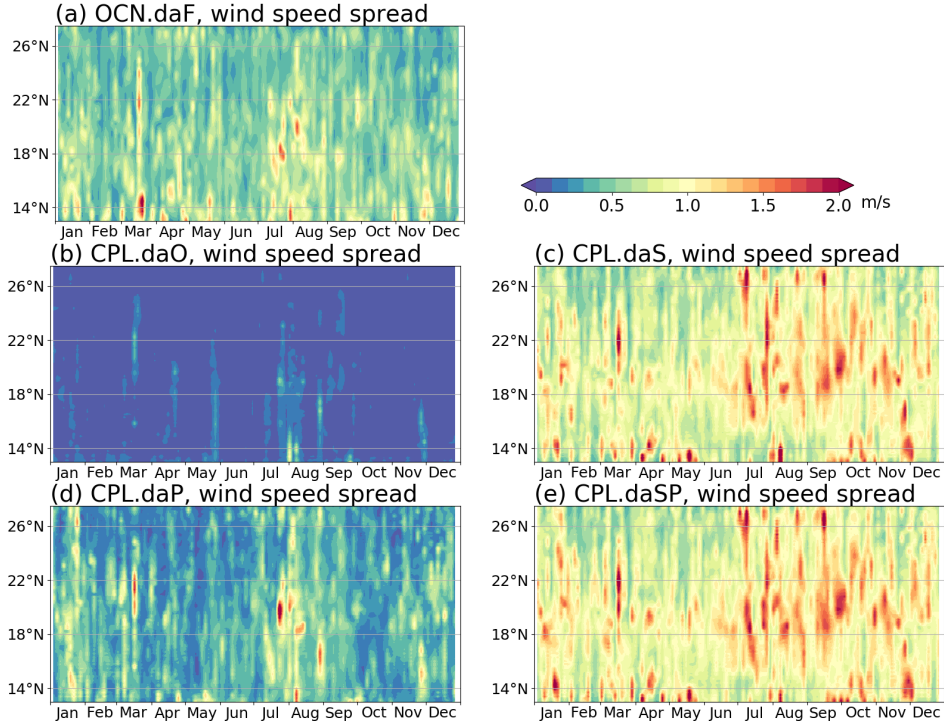


Figure 3. The spatial and temporal evolution of the RMS spread of 10-m wind speed along the center line of the Red Sea shown in Fig. 1(c). Panel (a) shows the spread from the ECMWF derived forcing; Panel (b-e) show the spread in the coupled experiments with no perturbations, only SKEB, only perturbed model physics, and SKEB + perturbed model physics, respectively.

361 SST analysis obtained in CPL.daSP has a slightly larger RMSE compared to that ob-
 362 tained in CPL.daF, but the differences between OCN.daF, CPL.daS, CPL.daP, and CPL.daSP
 363 are within 0.01°C (2%). In addition, the CPL.daSP also has the smallest distance be-
 364 tween the forecasts and analyses RMSEs, indicating less “assimilation shock” and more
 365 balanced ocean states in the DA experiment.

366 3.3 Sea Surface Height

367 The SSH fields as estimated in the DA experiments are presented in Fig. 7 and Ta-
 368 ble 5. Similar to the SST results, the coupled DA experiments exhibit smaller RMSE
 369 and larger spread. The SSH forecast errors in OCN.daF, CPL.daS, CPL.daP, and CPL.daSP
 370 are not significantly different. Although CPL.daSP still has the smallest RMSEs, the dif-
 371 ferences are within 1% and smaller than the standard errors (about 0.001 m). For the
 372 SSH analyses, on the other hand, the CPL.daS and CPL.daSP are more significantly im-
 373 proved (RMSEs are smaller by 10% compared with OCN.daF and CPL.daP) when SKEBS
 374 are used, suggesting that including the stochastic forcing in model parameters is the key
 375 for improvements. Note that the spread of surface wind forcing shown in Fig. 3 is greatly
 376 increased when using the stochastic forcing.

377 The temporal evolution of the SSH is also examined by comparing with CMEMS-
 378 L4 data, shown in Fig. 8. Here we only highlight the differences of the SSH analyses be-
 379 cause the forecasts are close to each other. Figure. 8 shows that the CPL.daSP exper-
 380 iment has larger correlations and smaller RMSEs in both the Red Sea and the Gulf of
 381 Aden regions. Similar to the results shown in Fig. 7, when using the stochastic forcings
 382 in WRF, CPL.daS and CPL.daSP outperform the uncoupled model OCN.daF (see Ta-
 383 ble 5).

Table 4. SST obtained in the DA experiments against the validation data. We highlighted the best forecast/analysis using red, but the pink color is used when the differences between uncoupled and coupled experiments are insignificant (when the RMSE difference is smaller than 5% or the standard error).

	OCN.daO	OCN.daF	CPL.daO	CPL.daS	CPL.daP	CPL.daSP
Against assimilated data						
SST forecast RMSE	0.656	0.486	0.500	0.419	0.426	0.403
SST analysis RMSE	0.475	0.341	0.374	0.281	0.294	0.262
Against OSTIA SST						
SST forecast RMSE	0.650	0.574	0.610	0.560	0.551	0.539
SST analysis RMSE	0.486	0.463	0.484	0.468	0.472	0.469
SST forecast correlation	0.9580	0.9623	0.9573	0.9637	0.9628	0.9649
SST analysis correlation	0.9786	0.9805	0.9773	0.9800	0.9788	0.9791
SST forecast spread	0.078	0.080	0.077	0.098	0.095	0.108
SST analysis spread	0.046	0.052	0.048	0.059	0.055	0.062

Table 5. Summary of SSH against the validation data. We highlighted the best forecast/analysis using red, but the pink color is used when the differences between coupled and uncoupled experiments are insignificant (when the RMSE difference is smaller than 5% or the standard error).

	OCN.daO	OCN.daF	CPL.daO	CPL.daS	CPL.daP	CPL.daSP
Against assimilated data						
SSH forecast RMSE	0.0646	0.0626	0.0650	0.0624	0.0626	0.0620
SSH analysis RMSE	0.0580	0.0495	0.0578	0.0446	0.0522	0.0433
Against CMEMS-L4 SSH						
SSH forecast RMSE	0.0513	0.0486	0.0513	0.0483	0.0494	0.0482
SSH analysis RMSE	0.0461	0.0390	0.0455	0.0356	0.0409	0.0350
SSH forecast correlation	0.9121	0.9197	0.9109	0.9197	0.9168	0.9204
SSH analysis correlation	0.9314	0.9493	0.0320	0.9578	0.9439	0.9590
SSH forecast spread	0.0034	0.0056	0.0036	0.0073	0.0048	0.0076
SSH analysis spread	0.0023	0.0038	0.0024	0.0046	0.0032	0.0047

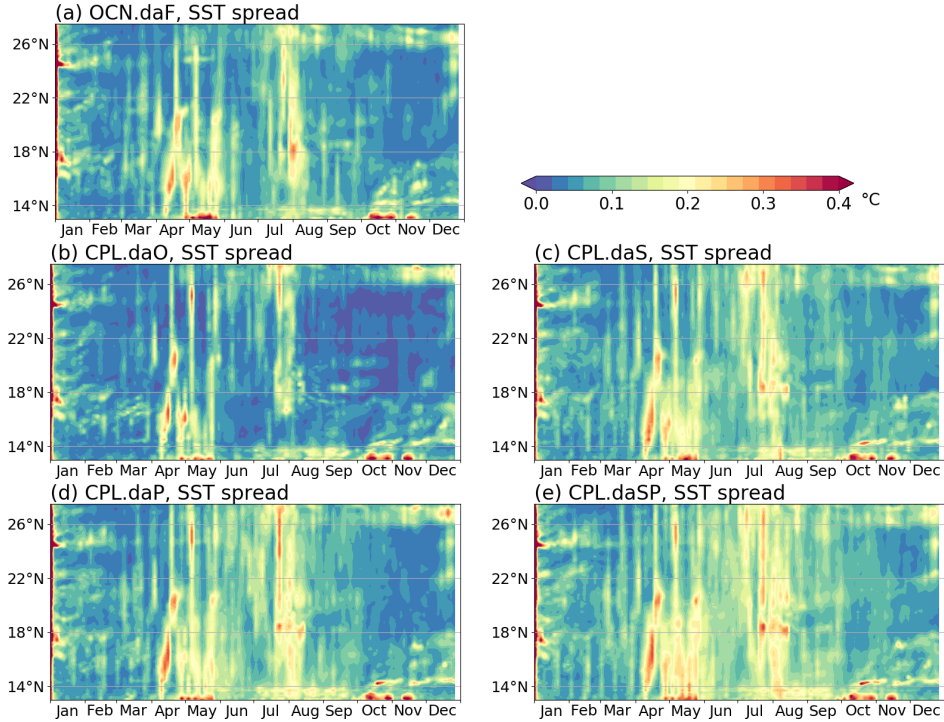


Figure 4. The spatial and temporal evolution of the RMS spread of Sea Surface Temperature along the center line of the Red Sea shown in Fig. 1(c). Panel (a) shows the spread in the ocean-only experiment driven by ECMWF derived forcing; Panel (b-e) show the spread in the coupled experiments with no perturbations, only SKEB, only perturbed model physics, and SKEB + perturbed model physics, respectively.

384

3.4 Temperature and Salinity Profiles

385

386

387

388

389

390

391

392

393

394

395

396

397

398

399

400

The subsurface features of the ocean are validated against independent (i.e. not assimilated) CTD observations of temperature and salinity from the WHOI/KAUST summer cruise in the Red Sea between September 15 and October 08 2011. The difference between daily averaged forecasts and observations is shown in Figs. 9 and 10. More than 2 degree and 0.8 psu differences are found for temperature and salinity profiles in the thermocline between 50–100 m. For the temperature profiles, the RMSE in CPL.daSP (0.361°C) is smaller than OCN.daO (0.408°C) by about 10%, especially near the ocean surface, but within 2% difference compared to OCN.daF, CPL.daO, and CPL.daS. For the salinity profiles, the forecast RMSE of CPL.daSP (0.082 psu) is smaller than the benchmark experiment OCN.daO by about 30%. It is noted that CPL.daP has the smallest RMSE for temperature (0.344°C), but its salinity RMSE is significantly larger (0.122 psu) than CPL.daSP. Compared with the ocean-only experiment OCN.daF, the RMSEs in CPL.daS and CPL.daSP are not significantly different (within 1% or 2%). Although the coupled experiment is no better than the best uncoupled experiment OCN.daF, the results indicate the stochastic schemes in WRF are crucial for producing better forecasts of the ocean profiles.

401

3.5 Feedback to the Atmosphere

402

403

404

405

406

To assess the impact of ocean data assimilation on the surface of the atmosphere, we compare the latent heat fluxes and 10-m wind speed obtained in the DA experiments. This analysis informs feedback to the heat and momentum fluxes. We consider ERA5 as reference and present the RMSEs of latent heat fluxes and 10-m wind speed in Fig. 11. Here we only compare the data on the centerline of the Red Sea to highlight ocean re-

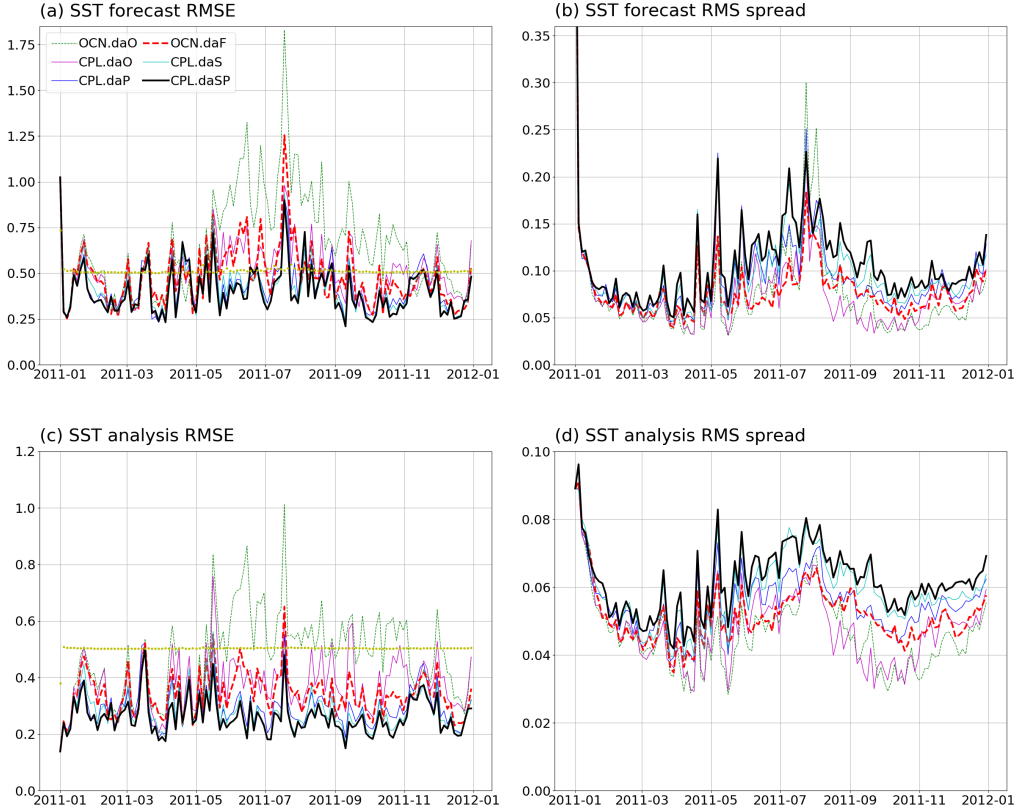


Figure 5. Time history of SST RMSEs and spreads during the data assimilation experiment. Panels (a) and (c) show the RMSEs of the forecasts and analyses against the assimilated data; Panels (b) and (d) show the spread of SST in the forecasts and analyses. The yellow dots in Panels (a) and (c) indicate the total uncertainty (square root of the sum of ensemble variance and observational variance $(0.5^{\circ}\text{C})^2$) of CPL.daSP.

407 regions. It can be seen that the RMSEs do not grow significantly with time, showing the
 408 capability of the coupled system for the 1-year DA experiments. We hypothesize this is
 409 because the atmospheric states are constrained by the boundary conditions for this relatively
 410 small domain. Compared with the benchmark case CPL.daO, the RMSEs of the latent heat flux
 411 and 10-m wind speed obtained from CPL.daSP are smaller by about 4%, but the RMSE differ-
 412 ences are smaller than the standard error, implying the improved ocean states may not significantly
 413 impact the atmospheric states. Because of the small differences in the surface atmosphere, this
 414 indicates that for the Red Sea region, the skill of the coupled model is not from the two-way
 415 coupling, but from the atmospheric forcings in the downscaled WRF ensembles (one-way coupled)
 416 to drive the ocean model.

417 3.6 Vertical Current Velocity

418 Toye et al. (2017) argued that the dynamical balances (or assimilation shock) in
 419 the oceanic model from the EAKF increments increase the spread of the Red Sea fore-
 420 casts. The imbalances are also reported in other EAKF assimilation experiments (L. A. An-
 421 derson et al., 2000; Hoteit et al., 2010; Park et al., 2018). Here, we investigate the dy-
 422 namical balances in our experiments by comparing the standard deviation of $|w|$ obtained
 423 in the DA experiments with the “free” run without assimilating observation data in Fig. 12.
 424 The results show that the spreads of $|w|$ in all DA experiments are larger than the “free”
 425 run for the Red Sea region, but there are no significant changes in $|w|$ spread when the

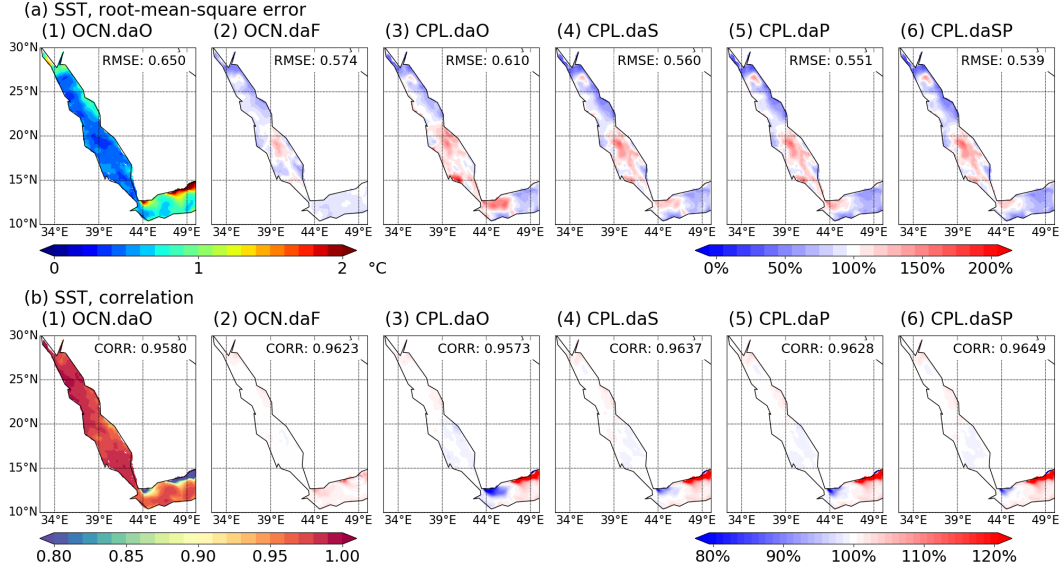


Figure 6. SST RMSEs and correlations obtained in the DA experiments validated against OSTIA. Panels (a) and (b) show the RMSE and correlation of the “forecast” SST. The contours in column 1 indicate the comparison with OSTIA data; columns 2-5 are normalized by the reference OCN.daO in column 1 to highlight differences, showing the ratios in percentage.

426 coupled model is used in comparison with ocean-only model experiments, indicating no
 427 significant dynamical imbalances.

428 4 Summary and Conclusions

429 This work implemented a data assimilation framework based on the regional cou-
 430 ppled model SKRIPS and DART. Using the EAKF in DART, we investigate the impact
 431 of ocean data assimilation on the oceanic and atmospheric states of the Red Sea. The
 432 coupled system assimilates satellite-based sea surface temperature and height and in situ
 433 temperature and salinity glider profiles every 3 days for 1 year starting from January 01,
 434 2011.

435 To assess the performance of the ensemble forecasts and examine the generated ocean
 436 states, we ran a series of experiments using different perturbation schemes. The assim-
 437 ilation results of the coupled experiments are compared with the uncoupled ones forced
 438 by ECMWF-derived surface forcing, revealing that the coupled experiments give greater
 439 spread in the ensembles of ocean states, with the spread continuing to increase when us-
 440 ing the stochastic kinetic energy backscatter (SKEB) scheme. Compared with the as-
 441 similated data, the coupled experiments result in a more skillful SST and SSH ensem-
 442 ble mean forecast. The SST forecasts and SSH analyses in coupled models are also bet-
 443 ter than uncoupled ones when compared with the independent observational data, but
 444 the RMSEs of SST analyses and SSH forecasts are insignificantly different.

445 We further compared the DA experiment results with the independent cruise ob-
 446 servation data of temperature and temperature profiles. The comparison shows large vari-
 447 ations in the temperature profiles because of the challenge in modeling the thermocline
 448 layer and the lack of in situ data. The RMSEs from the coupled DA experiments with
 449 perturbations of the atmospheric model are comparable to the uncoupled model driven
 450 by ECMWF-derived ensemble forcing, and both are better than the benchmark experi-
 451 ments with small spreads in atmospheric forcings. To investigate the feedback from the

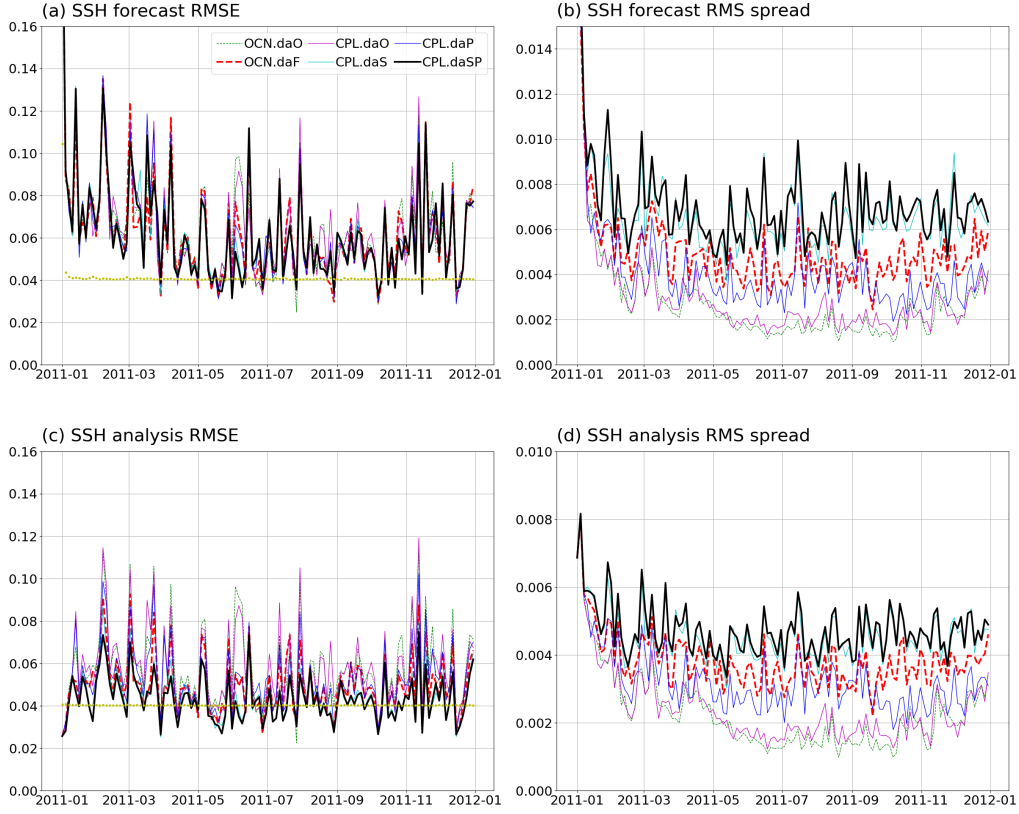


Figure 7. Evolution of the SSH RMSEs and spreads during the data assimilation experiment. Panels (a-b) show the RMSEs of the forecasts and analyses against the assimilated data; Panels (c-d) show the RMS spread of SSH in the forecasts and analyses. The yellow dots in Panels (a) and (c) indicate the total uncertainty (square root of the sum of ensemble variance and observational variance $(0.04 \text{ m})^2$) of CPL.daSP.

452 ocean, we validated the latent heat flux and 10 m winds in all coupled experiments us-
 453 ing ERA5 data, but no significant difference is observed.

454 This study demonstrates that our Red Sea DA system using two-way coupled model
 455 with WRF performs better or equal to an uncoupled model driven by ECMWF-derived
 456 ensemble surface forcing, showing a promising approach for forecasting the oceanic states
 457 or producing ocean analysis data. The dynamical imbalances in the coupled model are
 458 also not significantly different from the uncoupled model. The DA system implemented
 459 here explores the utility of a coupled DA system and studies of the ocean–atmosphere
 460 interactions using the analysis data.

461 **Acknowledgments**

462 We gratefully acknowledge the research funding (grant number: OSR-2022-NCM-4829.5)
 463 from KAUST (King Abdullah University of Science and Technology). We also appre-
 464 ciate the computational resources of the supercomputer Shaheen II and the assistance
 465 provided by KAUST Supercomputer Laboratory. RS and ACS were supported by ONR
 466 ASTRAL research initiative (N00014-23-1-2092). ACS was supported by NOAA Grant
 467 NA18OAR4310405 and ONR MISOBBOB research initiative (N00014-17-S-B001). BDC
 468 and MRM were supported by NOAA Grant NA21OAR4310257, NA18OAR4310403, and
 469 NA22OAR4310597. AJM was partly supported by the National Science Foundation (OCE-

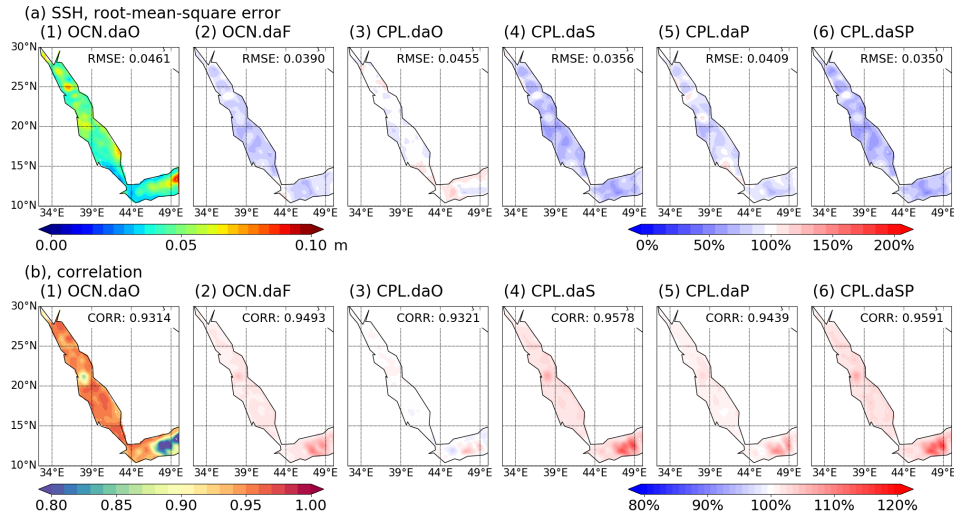


Figure 8. SSH RMSEs and correlations obtained in the DA experiments validated against CMEMS-L4 data. Panels (a) and (b) show the RMSEs and correlations of the SSH analyses. The contours in column 1 indicate the comparison with CMEMS-L4 data; columns 2-5 are normalized by the reference OCN.daO in column 1 to highlight differences, showing the ratios in percentage

2022868). We appreciate Luca Delle Monache, Daniel Steinhoff, and Rachel Weihs for discussing the generation of WRF ensembles.

Data Availability Statement

The coupled model used for the simulations is available at https://github.com/iurnus/scripps_kaust_model. The DA experimental results used in the paper are available at <https://zenodo.org/records/10408667>.

Author contributions statement

All authors conceived the experiments; R.S. implemented the DA system for the coupled models; S.S. implemented the DA system for the uncoupled models and the RO-COTO workflow; R.S. conducted the experiments and plotted the figures; R.S. and S.S. drafted the initial manuscript; all authors discussed the results and revised the manuscript.

Competing Interests

The authors declare no competing interests.

References

- Anderson, J., & Anderson, S. (1999). A Monte Carlo implementation of the nonlinear filtering problem to produce ensemble assimilations and forecasts. *Monthly Weather Review*, *127*(12), 2741–2758. doi: 10.1175/1520-0493(1999)127<2741:AMCIOT>2.0.CO;2
- Anderson, J., Hoar, T., Raeder, K., Liu, H., Collins, N., Torn, R., & Avellano, A. (2009). The Data Assimilation Research Testbed: A community facility. *Bulletin of the American Meteorological Society*, *90*(9), 1283–1296.
- Anderson, L. A., Robinson, A. R., & Lozano, C. J. (2000). Physical and biological modeling in the Gulf Stream region:: I. Data assimilation methodology. *Deep Sea Research Part I: Oceanographic Research Papers*, *47*(10), 1787–1827.

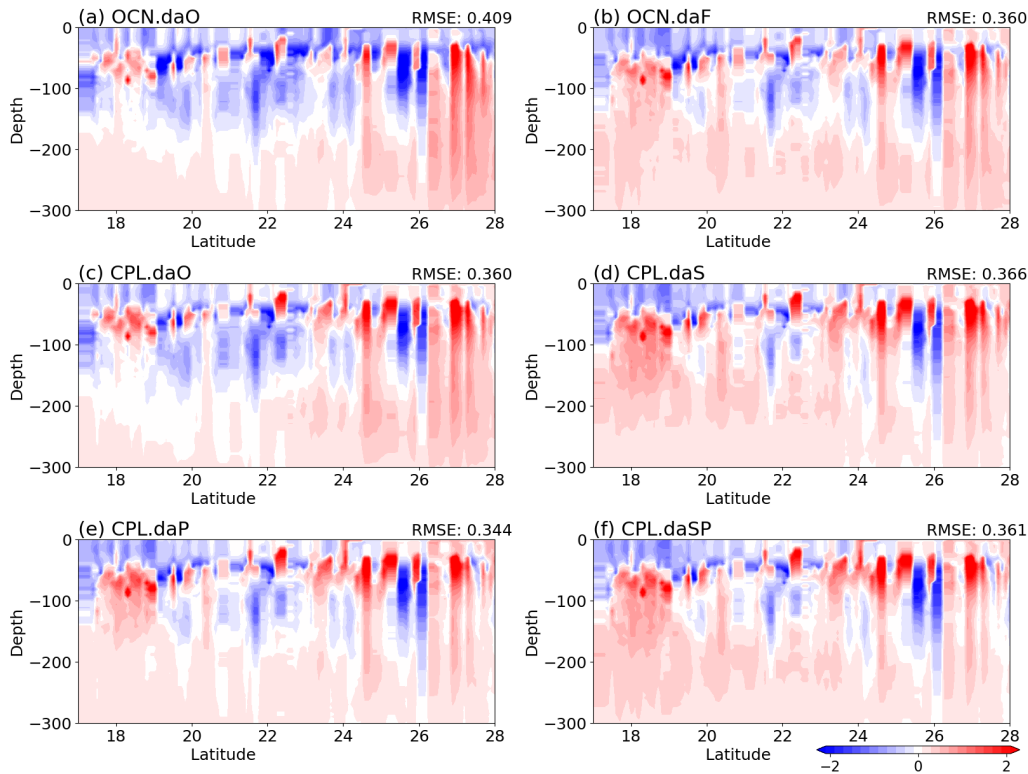


Figure 9. The differences between the temperature at 0–300 m obtained in the DA experiments compared to in situ observations (results minus observations).

- 494 Bannister, R. N. (2008a). A review of forecast error covariance statistics in at-
 495 mospheric variational data assimilation. I: Characteristics and measurements
 496 of forecast error covariances. *Quarterly Journal of the Royal Meteorological*
 497 *Society*, *134*(637, B), 1951–1970. doi: 10.1002/qj.339
- 498 Bannister, R. N. (2008b). A review of forecast error covariance statistics in atmo-
 499 spheric variational data assimilation. II: Modelling the forecast error covariance
 500 statistics. *Quarterly Journal of the Royal Meteorological Society*, *134*(637),
 501 1971–1996. doi: 10.1002/qj.340
- 502 Bannister, R. N. (2017). A review of operational methods of variational and
 503 ensemble-variational data assimilation. *Quarterly Journal of the Royal Me-*
 504 *teorological Society*, *143*(703), 607–633.
- 505 Banzon, V., Smith, T. M., Chin, T. M., Liu, C., & Hankins, W. (2016). A long-term
 506 record of blended satellite and in situ sea-surface temperature for climate mon-
 507 itoring, modeling and environmental studies. *Earth System Science Data*, *8*(1),
 508 165–176.
- 509 Berner, J., Fossell, K., Ha, S.-Y., Hacker, J., & Snyder, C. (2015). Increasing the
 510 skill of probabilistic forecasts: Understanding performance improvements from
 511 model-error representations. *Monthly Weather Review*, *143*(4), 1295–1320.
- 512 Berner, J., Ha, S.-Y., Hacker, J., Fournier, A., & Snyder, C. (2011). Model un-
 513 certainty in a mesoscale ensemble prediction system: Stochastic versus multi-
 514 physics representations. *Monthly Weather Review*, *139*(6), 1972–1995.
- 515 Berner, J., Shutts, G., Leutbecher, M., & Palmer, T. (2009). A spectral stochastic
 516 kinetic energy backscatter scheme and its impact on flow-dependent pre-
 517 dictability in the ECMWF ensemble prediction system. *Journal of the Atmo-*
 518 *spheric Sciences*, *66*(3), 603–626.
- 519 Bougeault, P., Toth, Z., Bishop, C., Brown, B., Burridge, D., Chen, D. H., ... others
 520 (2010). The THORPEX interactive grand global ensemble. *Bulletin of the*

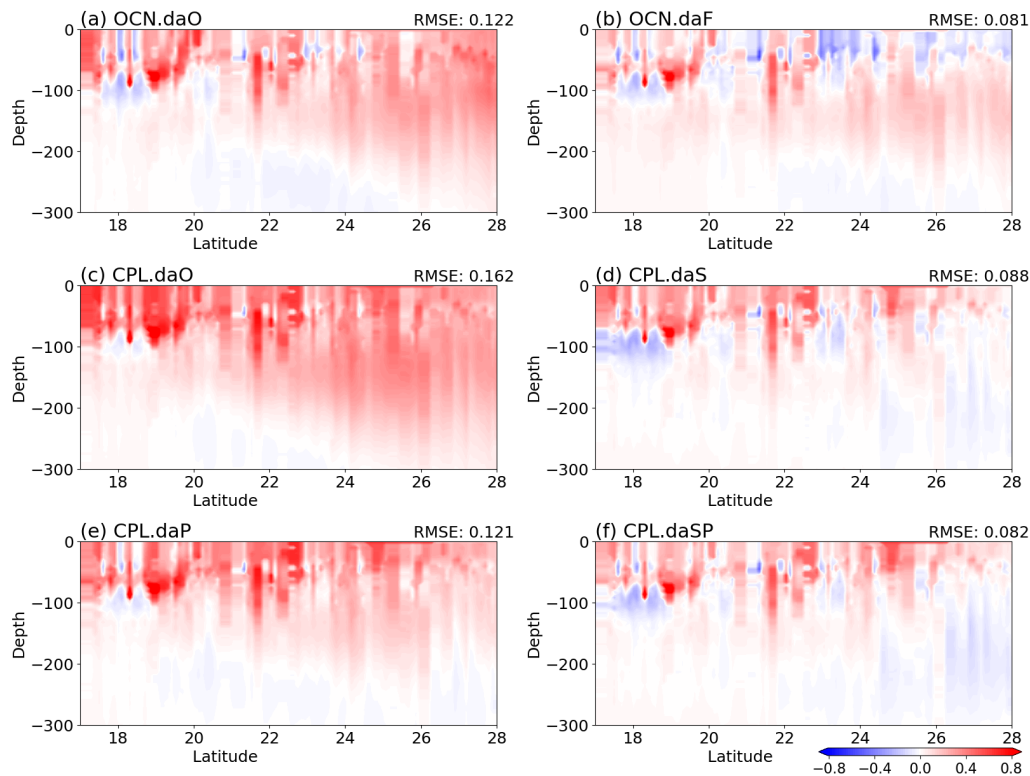


Figure 10. The differences between the salinity at 0-300 m obtained in the DA experiments in comparison with in situ observations (results minus observations).

- 521 *American Meteorological Society*, 91(8), 1059–1072.
- 522 Brankart, J.-M., Candille, G., Garnier, F., Calone, C., Melet, A., Bouttier, P.-A., ...
 523 Verron, J. (2015). A generic approach to explicit simulation of uncertainty in
 524 the NEMO ocean model. *Geoscientific Model Development*, 8(5), 1285-1297.
 525 doi: 10.5194/gmd-8-1285-2015
- 526 Buizza, R. (2014). *The TIGGE global, medium-range ensembles*. European Centre
 527 for Medium-Range Weather Forecasts.
- 528 Campin, J.-M., Heimbach, P., Losch, M., Forget, G., edhill3, Adcroft, A., ... T.,
 529 A. T. (2019). Mitgcm/mitgcm: checkpoint67m.
 530 doi: 10.5281/zenodo.3492298
- 531 Chen, S.-H., & Sun, W.-Y. (2002). A one-dimensional time dependent cloud model.
 532 *Journal of the Meteorological Society of Japan. Ser. II*, 80(1), 99–118.
- 533 Cox, M. (1987). Isopycnal diffusion in a z-coordinate ocean model. *Ocean modelling*,
 534 74, 1–5.
- 535 Danabasoglu, G., & McWilliams, J. (1995). Sensitivity of the global ocean circula-
 536 tion to parameterizations of mesoscale tracer transports. *Journal of Climate*,
 537 8(12), 2967-2987. doi: 10.1175/1520-0442(1995)008<2967:SOTGOC>2.0.CO;2
- 538 Dasari, H. P., Desamsetti, S., Langodan, S., Attada, R., Ashok, K., & Hoteit, I.
 539 (n.d.). Long-term changes in the Arabian Peninsula rainfall and their relation-
 540 ship with the ENSO signals in the tropical Indo-Pacific. *Climate Dynamics*,
 541 1–17.
- 542 Davis, S. R., Farrar, J. T., Weller, R. A., Jiang, H., & Pratt, L. J. (2019). The
 543 land-sea breeze of the Red Sea: observations, simulations, and relationships to
 544 regional moisture transport. *Journal of Geophysical Research: Atmospheres*,
 545 124(24), 13803–13825.
- 546 Donlon, C. J., Martin, M., Stark, J., Roberts-Jones, J., Fiedler, E., & Wimmer, W.
 547 (2012). The operational sea surface temperature and sea ice analysis (OSTIA)

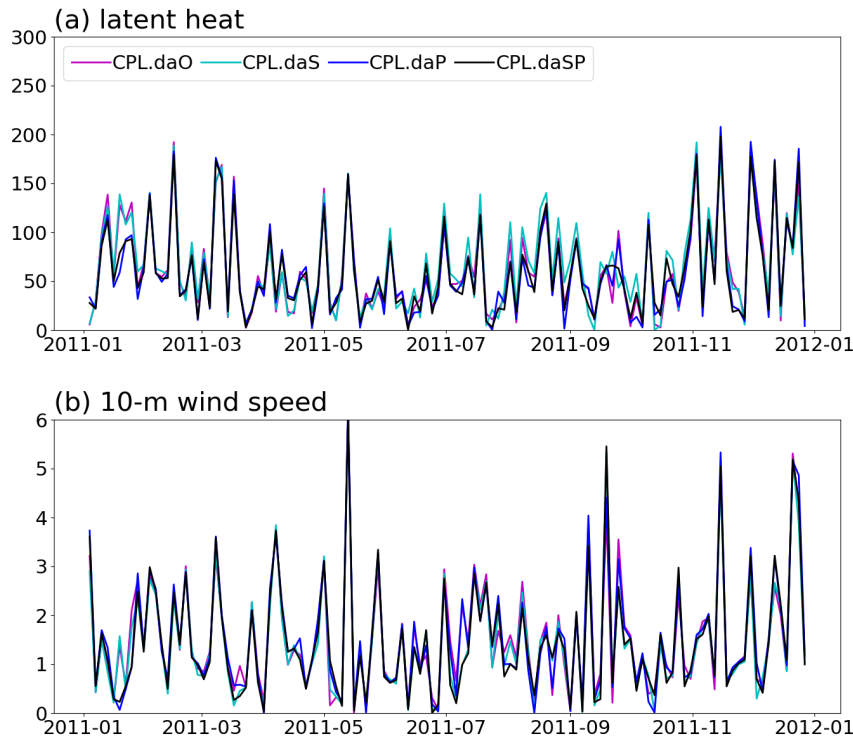


Figure 11. The RMSEs of latent heat flux and 10-m wind speed obtained in the coupled model when assimilating the ocean data. We only compare the data on the centerline of the Red Sea.

- 548 system. *Remote Sensing of Environment*, 116, 140–158.
- 549 Edwards, C. A., Moore, A. M., Hoteit, I., & Cornuelle, B. D. (2015). Regional
 550 ocean data assimilation. In C. Carlson & S. Giovannoni (Eds.),
 551 *Annual review of marine science*, vol 7 (Vol. 7, p. 21-42). doi: 10.1146/
 552 annurev-marine-010814-015821
- 553 Evensen, G. (1994). Sequential data assimilation with a nonlinear quasi-geostrophic
 554 model using Monte Carlo methods to forecast error statistics. *Journal of Geo-*
 555 *physical Research: Oceans*, 99(C5), 10143–10162.
- 556 Evensen, G. (2003). The ensemble Kalman filter: Theoretical formulation and practical
 557 implementation. *Ocean dynamics*, 53, 343–367.
- 558 Evensen, G. (2004). Sampling strategies and square root analysis schemes for the
 559 enfk. *Ocean Dynamics*, 54(6), 539–560. doi: 10.1007/s10236-004-0099-2
- 560 Evensen, G., & Van Leeuwen, P. J. (1996). Assimilation of Geosat altimeter data for
 561 the Agulhas current using the ensemble Kalman filter with a quasigeostrophic
 562 model. *Monthly Weather Review*, 124(1), 85–96.
- 563 Fairall, C., Bradley, E. F., Hare, J., Grachev, A., & Edson, J. (2003). Bulk pa-
 564 rameterization of air–sea fluxes: Updates and verification for the COARE
 565 algorithm. *Journal of Climate*, 16(4), 571–591.
- 566 Gaspar, P., Gregoris, Y., & Lefevre, J. (1990). A simple eddy kinetic-energy model
 567 for simulations of the oceanic vertical mixing - Tests at station Papa and long-
 568 term upper ocean study site. *Journal of Geophysical Research-Oceans*, 95(C9),
 569 16179–16193. doi: 10.1029/JC095iC09p16179
- 570 Gent, P., & McWilliams, J. (1990). Isopycnal mixing in ocean circulation mod-
 571 els. *Journal of Physical Oceanography*, 20(1), 150–155. doi: 10.1175/1520-
 572 -0485(1990)020(0150:IMIOCM)2.0.CO;2

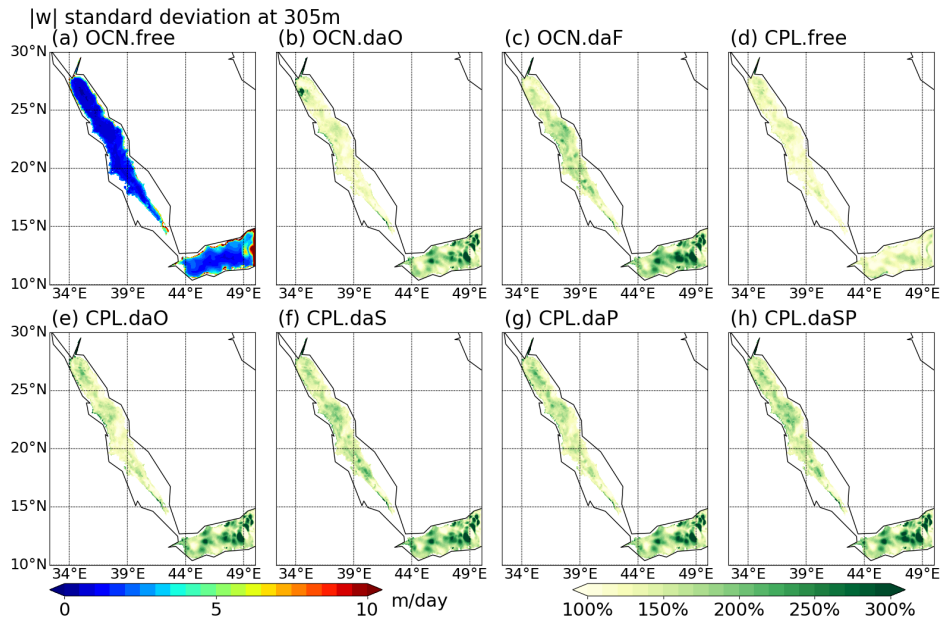


Figure 12. Standard deviation of $|w|$ at 300 m obtained in the DA experiments. Panels (b)-(h) are normalized by the reference OCN.free in panel (a) to highlight differences.

- 573 Gent, P., Willebrand, J., Mcdougall, T., & McWilliams, J. (1995). Parameterizing
 574 eddy-induced tracer transports in ocean circulation models. *Journal of Phys-*
 575 *ical Oceanography*, 25(4), 463-474. doi: 10.1175/1520-0485(1995)025<0463:
 576 PEITTI>2.0.CO;2
- 577 Good, S. A., Martin, M. J., & Rayner, N. A. (2013). EN4: Quality controlled
 578 ocean temperature and salinity profiles and monthly objective analyses with
 579 uncertainty estimates. *Journal of Geophysical Research: Oceans*, 118(12),
 580 6704–6716.
- 581 Grell, G. A., & Freitas, S. R. (2014). A scale and aerosol aware stochastic convective
 582 parameterization for weather and air quality modeling. *Atmospheric Chemistry*
 583 *and Physics*, 14(10), 5233–5250.
- 584 Griffies, S., & Hallberg, R. (2000). Biharmonic friction with a smagorinsky-
 585 like viscosity for use in large-scale eddy-permitting ocean models. *Monthly*
 586 *Weather Review*, 128(8, 2), 2935-2946. doi: 10.1175/1520-0493(2000)128<2935:
 587 BFWASL>2.0.CO;2
- 588 Harrop, C., samtrahan, christinaholt, & Brown, T. (2017, Sep). christopherwhar-
 589 rop/rocoto: Rocoto 1.2.4.
 590 doi: 10.5281/zenodo.890939
- 591 Hill, C., DeLuca, C., Balaji, Suarez, M., & Silva, A. (2004). The architecture of the
 592 earth system modeling framework. *Computing in Science & Engineering*, 6(1),
 593 18–28.
- 594 Holland, W. (1978). Role of mesoscale eddies in general circulation of ocean - nu-
 595 merical experiments using a wind-driven quasi-geostrophic model. *Journal of*
 596 *Physical Oceanography*, 8(3), 363-392. doi: 10.1175/1520-0485(1978)008<0363:
 597 TROMEI>2.0.CO;2
- 598 Hong, S.-Y., & Lim, J.-O. J. (2006). The WRF single-moment 6-class microphysics
 599 scheme (WSM6). *Asia-Pacific Journal of Atmospheric Sciences*, 42(2), 129–
 600 151.
- 601 Hong, S.-Y., Noh, Y., & Dudhia, J. (2006). A new vertical diffusion package with an
 602 explicit treatment of entrainment processes. *Monthly Weather Review*, 134(9),
 603 2318–2341.

- 604 Hoteit, I., Abualnaja, Y., Afzal, S., Ait-El-Fquih, B., Akylas, T., Antony, C., ...
605 Zodiatis, G. (2021). Towards an end-to-end analysis and prediction sys-
606 tem for weather, climate, and marine applications in the Red Sea. *Bul-*
607 *letin of the American Meteorological Society*, 102(1), E99 - E122. Re-
608 trieved from [https://journals.ametsoc.org/view/journals/bams/102/](https://journals.ametsoc.org/view/journals/bams/102/1/BAMS-D-19-0005.1.xml)
609 [1/BAMS-D-19-0005.1.xml](https://journals.ametsoc.org/view/journals/bams/102/1/BAMS-D-19-0005.1.xml) doi: <https://doi.org/10.1175/BAMS-D-19-0005.1>
- 610 Hoteit, I., Cornuelle, B., & Heimbach, P. (2010). An eddy-permitting, dynamically
611 consistent adjoint-based assimilation system for the tropical Pacific: Hindcast
612 experiments in 2000. *Journal of Geophysical Research: Oceans*, 115(C3).
- 613 Hoteit, I., Hoar, T., Gopalakrishnan, G., Collins, N., Anderson, J., Cornuelle, B.,
614 ... Heimbach, P. (2013). A MITgcm/DART ensemble analysis and prediction
615 system with application to the Gulf of Mexico. *Dynamics of Atmospheres and*
616 *Oceans*, 63, 1–23.
- 617 Hoteit, I., Pham, D., & Blum, J. (2002). A simplified reduced order Kalman filter-
618 ing and application to altimetric data assimilation in Tropical Pacific. *Journal*
619 *of Marine Systems*, 36(1-2), 101-127. doi: 10.1016/S0924-7963(02)00129-X
- 620 Hoteit, I., Pham, D.-T., Gharamti, M., & Luo, X. (2015). Mitigating observa-
621 tion perturbation sampling errors in the stochastic EnKF. *Monthly Weather*
622 *Review*, 143(7), 2918–2936.
- 623 Houtekamer, P. L., Mitchell, H. L., Pellerin, G., Buehner, M., Charron, M., Spacek,
624 L., & Hansen, B. (2005). Atmospheric data assimilation with an ensem-
625 ble Kalman filter: Results with real observations. *Monthly Weather Review*,
626 133(3), 604–620.
- 627 Iacono, M. J., Delamere, J. S., Mlawer, E. J., Shephard, M. W., Clough, S. A., &
628 Collins, W. D. (2008). Radiative forcing by long-lived greenhouse gases: Cal-
629 culations with the AER radiative transfer models. *Journal of Geophysical*
630 *Research: Atmospheres*, 113(D13).
- 631 Ingleby, B., & Huddleston, M. (2007). Quality control of ocean temperature and
632 salinity profiles—Historical and real-time data. *Journal of Marine Systems*,
633 65(1-4), 158–175.
- 634 Janjić, Z. I. (1994). The step-mountain eta coordinate model: Further developments
635 of the convection, viscous sublayer, and turbulence closure schemes. *Monthly*
636 *Weather Review*, 122(5), 927–945.
- 637 Jean-Michel, L., Eric, G., Romain, B.-B., Gilles, G., Angélique, M., Marie, D., ...
638 others (2021). The Copernicus global 1/12 oceanic and sea ice GLORYS12
639 reanalysis. *Frontiers in Earth Science*, 9, 698876.
- 640 Kain, J. S. (2004). The kain–fritsch convective parameterization: an update. *Journal*
641 *of applied meteorology*, 43(1), 170–181.
- 642 Karspeck, A. R., Yeager, S., Danabasoglu, G., Hoar, T., Collins, N., Raeder, K.,
643 ... Tribbia, J. (2013). An ensemble adjustment Kalman filter for the
644 CCSM4 ocean component. *Journal of Climate*, 26(19), 7392-7413. doi:
645 10.1175/JCLI-D-12-00402.1
- 646 Kwon, K. M., Choi, B.-J., Lee, S.-H., Kim, Y. H., Seo, G.-H., & Cho, Y.-K. (2016).
647 Effect of model error representation in the Yellow and East China Sea mod-
648 eling system based on the ensemble Kalman filter. *Ocean Dynamics*, 66(2),
649 263-283. doi: 10.1007/s10236-015-0909-8
- 650 Kwon, Y. C., & Hong, S.-Y. (2017). A mass-flux cumulus parameterization scheme
651 across gray-zone resolutions. *Monthly Weather Review*, 145(2), 583–598.
- 652 Langodan, S., Cavaleri, L., Vishwanadhapalli, Y., Pomaro, A., Bertotti, L., &
653 Hoteit, I. (2017). The climatology of the Red Sea—part 1: the wind. *Inter-*
654 *national Journal of Climatology*, 37(13), 4509–4517.
- 655 Large, W., Danabasoglu, G., Doney, S., & McWilliams, J. (1997). Sensitivity to
656 surface forcing and boundary layer mixing in a global ocean model: Annual-
657 mean climatology. *Journal of Physical Oceanography*, 27(11), 2418-2447. doi:
658 10.1175/1520-0485(1997)027<2418:STSFA2>2.0.CO;2

- 659 Large, W. G., McWilliams, J. C., & Doney, S. C. (1994). Oceanic vertical mixing: A
660 review and a model with a nonlocal boundary layer parameterization. *Reviews*
661 *of Geophysics*, *32*(4), 363–403.
- 662 Lawson, W., & Hansen, J. (2004). Implications of stochastic and determinis-
663 tic filters as ensemble-based data assimilation methods in varying regimes
664 of error growth. *Monthly Weather Review*, *132*(8), 1966–1981. doi:
665 10.1175/1520-0493(2004)132<1966:IOSADF>2.0.CO;2
- 666 Leeuwenburgh, O., Evensen, G., & Bertino, L. (2005). The impact of ensemble filter
667 definition on the assimilation of temperature profiles in the tropical Pacific.
668 *Quarterly Journal of the Royal Meteorological Society*, *131*(613, C), 3291–3300.
669 doi: 10.1256/qj.05.90
- 670 Leith, C. (1996). Stochastic models of chaotic systems. *PHYSICA D*, *98*(2-4),
671 481–491. (15th Annual International Conference of the Center-for-Nonlinear-
672 Studies on Nonlinear Phenomena in Ocean Dynamics, LOS ALAMOS, NM,
673 MAY 15-19, 1995) doi: 10.1016/0167-2789(96)00107-8
- 674 Lim, K.-S. S., & Hong, S.-Y. (2010). Development of an effective double-moment
675 cloud microphysics scheme with prognostic cloud condensation nuclei (CCN)
676 for weather and climate models. *Monthly Weather Review*, *138*(5), 1587–1612.
- 677 Lima, L. N., Pezzi, L. P., Penny, S. G., & Tanajura, C. A. S. (2019). An investiga-
678 tion of ocean model uncertainties through ensemble forecast experiments in the
679 southwest Atlantic Ocean. *Journal of Geophysical Research-Oceans*, *124*(1),
680 432–452. doi: 10.1029/2018JC013919
- 681 Lisæter, K. A., Rosanova, J., & Evensen, G. (2003). Assimilation of ice concen-
682 tration in a coupled ice–ocean model, using the ensemble Kalman filter. *Ocean*
683 *Dynamics*, *53*(4), 368–388.
- 684 Liu, P., Tsimpidi, A., Hu, Y., Stone, B., Russell, A., & Nenes, A. (2012). Differences
685 between downscaling with spectral and grid nudging using WRF. *Atmospheric*
686 *Chemistry and Physics*, *12*(8), 3601–3610.
- 687 Luo, X., & Hoteit, I. (2012). Ensemble Kalman filtering with residual nudging. *Tel-
688 lus A: Dynamic Meteorology and Oceanography*, *64*(1), 17130.
- 689 Marshall, J., Adcroft, A., Hill, C., Perelman, L., & Heisey, C. (1997). A finite-
690 volume, incompressible Navier Stokes model for studies of the ocean on parallel
691 computers. *Journal of Geophysical Research: Oceans*, *102*(C3), 5753–5766.
- 692 Mellor, G., & Yamada, T. (1982). Development of a turbulence closure-model for
693 geophysical fluid problems. *Reviews of Geophysics*, *20*(4), 851–875. doi: 10
694 .1029/RG020i004p00851
- 695 Mertz, F., Rosmorduc, V., Maheu, C., & Faugère, Y. (2017). *Product user manual,
696 For sea level SLA products.*
- 697 Morrison, H., Thompson, G., & Tatarskii, V. (2009). Impact of cloud microphysics
698 on the development of trailing stratiform precipitation in a simulated squall
699 line: Comparison of one-and two-moment schemes. *Monthly Weather Review*,
700 *137*(3), 991–1007.
- 701 Nakanishi, M., & Niino, H. (2004). An improved Mellor–Yamada level-3 model with
702 condensation physics: Its design and verification. *Boundary-Layer Meteorology*,
703 *112*(1), 1–31.
- 704 Nakanishi, M., & Niino, H. (2009). Development of an improved turbulence closure
705 model for the atmospheric boundary layer. *Journal of the Meteorological Soci-
706 ety of Japan. Ser. II*, *87*(5), 895–912.
- 707 Oakley, N. S., Liu, T., McGuire, L. A., Simpson, M., Hatchett, B. J., Tardy, A., ...
708 Steinhoff, D. (2023). Toward probabilistic post-fire debris-flow hazard decision
709 support. *Bulletin of the American Meteorological Society*.
- 710 Pacanowski, R., & Philander, S. (1981). Parameterization of vertical mixing in nu-
711 merical models of tropical oceans. *Journal of Physical Oceanography*, *11*(11),
712 1443–1451.

- 713 Park, J.-Y., Stock, C. A., Yang, X., Dunne, J. P., Rosati, A., John, J., & Zhang, S.
 714 (2018). Modeling global ocean biogeochemistry with physical data assimila-
 715 tion: a pragmatic solution to the equatorial instability. *Journal of Advances in*
 716 *Modeling Earth Systems*, 10(3), 891–906.
- 717 Penny, S. G., Behringer, D. W., Carton, J. A., & Kalnay, E. (2015). A hybrid global
 718 ocean data assimilation system at NCEP. *Monthly Weather Review*, 143(11),
 719 4660-4677. doi: 10.1175/MWR-D-14-00376.1
- 720 Prakash, P. J., Stenchikov, G., Kalenderski, S., Osipov, S., & Bangalath, H. (2014).
 721 The impact of dust storms on the Arabian Peninsula and the Red Sea. *Atmo-*
 722 *spheric Chemistry & Physics Discussions*, 14(13).
- 723 Redi, M. (1982). Oceanic isopycnal mixing by coordinate rotation. *Journal of Phys-*
 724 *ical Oceanography*, 12(10), 1154-1158. doi: 10.1175/1520-0485(1982)012<1154:
 725 OIMBCR>2.0.CO;2
- 726 Reynolds, R. W., Smith, T. M., Liu, C., Chelton, D. B., Casey, K. S., & Schlax,
 727 M. G. (2007). Daily high-resolution-blended analyses for sea surface tempera-
 728 ture. *Journal of climate*, 20(22), 5473–5496.
- 729 Sakov, P., Counillon, F., Bertino, L., Lisæter, K., Oke, P., & Korablev, A. (2012).
 730 Topaz4: an ocean-sea ice data assimilation system for the North Atlantic and
 731 Arctic. *Ocean Science*, 8(4), 633–656.
- 732 Sandery, P. A., Sakov, P., & Majewski, L. (2014). The impact of open boundary
 733 forcing on forecasting the east australian current using ensemble data assimila-
 734 tion. *Ocean Modelling*, 84, 1-11. doi: 10.1016/j.ocemod.2014.09.005
- 735 Sanikommu, S., Banerjee, D. S., Baduru, B., Paul, B., Paul, A., Chakraborty, K.,
 736 & Hoteit, I. (2019). Impact of dynamical representational errors on an in-
 737 dian ocean ensemble data assimilation system. *Quarterly Journal of the Royal*
 738 *Meteorological Society*, 145(725), 3680–3691.
- 739 Sanikommu, S., Langodan, S., Dasari, H. P., Zhan, P., Krokos, G., Abualnaja, Y. O.,
 740 ... Hoteit, I. (2023a). Making the case for high resolution regional ocean
 741 reanalyses: An example with the Red Sea. *Bulletin of the American Meteorolo-*
 742 *gical Society*, E1241–E1264.
- 743 Sanikommu, S., Langodan, S., Dasari, H. P., Zhan, P., Krokos, G., Abualnaja,
 744 Y. O., ... Hoteit, I. (2023b). Making the case for high-resolution regional
 745 ocean reanalyses: An example with the Red Sea. *Bulletin of the American*
 746 *Meteorological Society*, 104(7), E1241 - E1264. Retrieved from [https://](https://journals.ametsoc.org/view/journals/bams/104/7/BAMS-D-21-0287.1.xml)
 747 journals.ametsoc.org/view/journals/bams/104/7/BAMS-D-21-0287.1.xml
 748 doi: <https://doi.org/10.1175/BAMS-D-21-0287.1>
- 749 Sanikommu, S., Paul, A., Sluka, T., Ravichandran, M., & Kalnay, E. (2017). The
 750 pre-argo ocean reanalyses may be seriously affected by the spatial coverage of
 751 moored buoys. *SCIENTIFIC REPORTS*, 7. doi: 10.1038/srep46685
- 752 Sanikommu, S., Toye, H., Zhan, P., Langodan, S., Krokos, G., Knio, O., & Hoteit,
 753 I. (2020). Impact of atmospheric and model physics perturbations on a
 754 high-resolution ensemble data assimilation system of the Red Sea. *Journal of*
 755 *Geophysical Research: Oceans*, 125(8), e2019JC015611.
- 756 Shu, Y., Zhu, J., Wang, D., & Xiao, X. (2011). Assimilating remote sensing and
 757 in situ observations into a coastal model of northern South China Sea using
 758 ensemble Kalman filter. *Continental Shelf Research*, 31(6, S, SI), S24-S36. doi:
 759 10.1016/j.csr.2011.01.017
- 760 Shutts, G. (2005). A kinetic energy backscatter algorithm for use in ensemble pre-
 761 diction systems. *Quarterly Journal of the Royal Meteorological Society: A*
 762 *journal of the atmospheric sciences, applied meteorology and physical oceanog-*
 763 *raphy*, 131(612), 3079–3102.
- 764 Skamarock, W. C., Klemp, J. B., Dudhia, J., Gill, D. O., Liu, Z., Berner, J., ...
 765 others (2019). A description of the advanced research WRF model version
 766 4. *National Center for Atmospheric Research: Boulder, CO, USA*, 145(145),
 767 550.

- 768 Smagorinsky, J., Galperin, B., & Orszag, S. (1993). Large eddy simulation of com-
 769 plex engineering and geophysical flows. *Evolution of physical oceanography*, 3–
 770 36.
- 771 Song, H., Hoteit, I., Cornuelle, B. D., & Subramanian, A. C. (2010). An adap-
 772 tive approach to mitigate background covariance limitations in the ensemble
 773 Kalman filter. *Monthly Weather Review*, 138(7), 2825–2845.
- 774 Stark, J. D., Donlon, C. J., Martin, M. J., & McCulloch, M. E. (2007). OSTIA: An
 775 operational, high resolution, real time, global sea surface temperature analysis
 776 system. In *Oceans 2007-europe* (pp. 1–4).
- 777 Sun, R., Cobb, A., Villas Bôas, A. B., Langodan, S., Subramanian, A. C., Mazloff,
 778 M. R., . . . Hoteit, I. (2023). Waves in SKRIPS: WAVEWATCH III coupling
 779 implementation and a case study of tropical cyclone mekunu. *Geoscientific*
 780 *Model Development*, 16(12), 3435–3458.
- 781 Sun, R., Subramanian, A. C., Miller, A. J., Mazloff, M. R., Hoteit, I., & Cornuelle,
 782 B. D. (2019). SKRIPS v1.0: a regional coupled ocean–atmosphere modeling
 783 framework (MITgcm–WRF) using ESMF/NUOPC, description and prelim-
 784 inary results for the Red Sea. *Geoscientific Model Development*, 12(10),
 785 4221–4244. doi: 10.5194/gmd-12-4221-2019
- 786 Tewari, M., Chen, F., Wang, W., Dudhia, J., LeMone, M., Mitchell, K., . . . Cuenca,
 787 R. (2004). Implementation and verification of the unified NOAA land sur-
 788 face model in the WRF model. In *20th conference on weather analysis and*
 789 *forecasting/16th conference on numerical weather prediction* (Vol. 1115).
- 790 Thompson, G., Field, P. R., Rasmussen, R. M., & Hall, W. D. (2008). Explicit fore-
 791 casts of winter precipitation using an improved bulk microphysics scheme. Part
 792 II: Implementation of a new snow parameterization. *Monthly Weather Review*,
 793 136(12), 5095–5115.
- 794 Toye, H., Zhan, P., Gopalakrishnan, G., Kartadikaria, A. R., Huang, H., Knio, O.,
 795 & Hoteit, I. (2017). Ensemble data assimilation in the Red Sea: sensitivity to
 796 ensemble selection and atmospheric forcing. *Ocean Dynamics*, 67(7), 915–933.
 797 doi: 10.1007/s10236-017-1064-1
- 798 Vandenbulcke, L., & Barth, A. (2015). A stochastic operational forecasting system
 799 of the Black Sea: Technique and validation. *Ocean Modelling*, 93, 7–21. doi: 10
 800 .1016/j.ocemod.2015.07.010
- 801 Wan, L., Zhu, J., Bertino, L., & Wang, H. (2008). Initial ensemble generation and
 802 validation for ocean data assimilation using HYCOM in the Pacific. *Ocean Dy-*
 803 *namics*, 58, 81–99.
- 804 Whitaker, J. S., & Hamill, T. M. (2012). Evaluating methods to account for system
 805 errors in ensemble data assimilation. *Monthly Weather Review*, 140(9), 3078–
 806 3089. doi: 10.1175/MWR-D-11-00276.1
- 807 Zhai, P., Bower, A. S., Smethie Jr, W. M., & Pratt, L. J. (2015). Formation and
 808 spreading of Red Sea outflow water in the Red Sea. *Journal of Geophysical Re-*
 809 *search: Oceans*, 120(9), 6542–6563.
- 810 Zhang, C., & Wang, Y. (2017). Projected future changes of tropical cyclone activity
 811 over the western North and South Pacific in a 20-km-mesh regional climate
 812 model. *Journal of Climate*, 30(15), 5923–5941.
- 813 Zhang, F., Snyder, C., & Sun, J. (2004). Impacts of initial estimate and ob-
 814 servation availability on convective-scale data assimilation with an ense-
 815 mble Kalman filter. *Monthly Weather Review*, 132(5), 1238–1253. doi:
 816 10.1175/1520-0493(2004)132<1238:IOIEAO>2.0.CO;2